Journal of South American Earth Sciences 117 (2022) 103887

Contents lists available at ScienceDirect

Journal of South American Earth Sciences

journal homepage: www.elsevier.com/locate/jsames

Source mechanisms and rupture processes of the Jujuy seismic nest, Chile-Argentina border

C. Valenzuela-Malebrán [a,b,*], S. Cesca [a], J.A. López-Comino [c,d], M. Zeckra [e], F. Krüger [b], T. Dahm [a,b]

[a] Helmholtz-Zentrum Potsdam Deutsches GeoForschungsZentrum, Potsdam, Germany
[b] Institute of Earth and Environmental Sciences, University of Potsdam, Potsdam, Germany
[c] Instituto Andaluz de Geofísica, Universidad de Granada, Granada, Spain
[d] Departamento de Física Teórica y Del Cosmos, Universidad de Granada, Granada, Spain
[e] Royal Observatory of Belgium, Avenue Circulaire 3, 1180 Uccle, Belgium

ARTICLE INFO

Keywords:
Seismic nest
Intermediate-deep earthquakes
Cluster analysis moment tensor inversion
directivity analysis

ABSTRACT

The Altiplano-Puna plateau, in Central Andes, is the second-largest continental plateau on Earth, extending between 22° and 27°S at an average altitude of 4400 m. The Puna plateau has been formed in consequence of the subduction of the oceanic Nazca Plate beneath the continental South American plate, which has an average crustal thickness of 50 km at this location. A large seismicity cluster, the Jujuy cluster, is observed at depth of 150–250 km beneath the central region of the Puna plateau. The cluster is seismically very active, with hundreds of earthquakes reported and a peak magnitude M_W 6.6 on 25th August 2006. The cluster is situated in one of three band of intermediate-depth focus seismicity, which extend parallel to the trench roughly North to South. It has been hypothesized that the Jujuy cluster could be a seismic nest, a compact seismogenic region characterized by a high stationary activity relative to its surroundings. In this study, we collected more than 40 years of data from different catalogs and proof that the cluster meets the three conditions of a seismic nest. Compared to other known intermediate depth nests at Hindu Kush (Afganisthan) or Bucaramanga (Colombia), the Jujuy nest presents an outstanding seismicity rate, with more than 100 M4+ earthquakes per year. We additionally performed a detailed analysis of the rupture process of some of the largest earthquakes in the nest, by means of moment tensor inversion and directivity analysis. We focused on the time period 2017–2018, where the seismic monitoring was the most extended. Our results show that earthquakes in the nest take place within the eastward subducting oceanic plate, but rupture along sub-horizontal planes dipping westward. We suggest that seismicity at Jujuy nest is controlled by dehydration processes, which are also responsible for the generation of fluids ascending to the crust beneath the Puna volcanic region. We use the rupture plane and nest geometry to provide a constraint to maximal expected magnitude, which we estimate as M_W ~6.7.

1. Introduction

In the central Andes, the convergence of the oceanic Nazca and continental South American plates shows a convergence rate of 68 mm/yr in a N76°E direction (Angermann et al., 1999) and the subducted Nazca plate dips moderately at an average angle of 30° at 100 km depth (Contreras-Reyes et al., 2021). Approximately 80–100 km eastward of the plate margin, the tectonic configuration led to the formation of the ~4 km high Altiplano-Puna plateau, the second-largest continental plateau on earth and it is the first continental plateau in a subduction regime, whereas the southern part, the Puna plateau exhibits a higher altitude of ~4,500 m with more rugged relief. Beneath the Altiplano-Puna plateau, the crust reaches almost 70 km in thickness (Yuan et al., 2000; Heit et al., 2014). The seismicity lies sub-parallel to the plate margin and can be divided into three depth bands of different spatial distribution and seismicity rate (Fig. 1). The first, most shallow band of seismicity, with depths down to 50–55 km, is located below the Chilean coast and characterized by a majority of interslab thrust earthquakes, which include megathrust earthquakes at shallow depth (~10–55 km). Among the most significant earthquakes in the region, we

* Corresponding author. Section 2.1, Physics of Earthquakes and Volcanoes, GFZ German Research Centre for Geosciences, Potsdam, Germany.
E-mail address: carlav@gfz-potsdam.de (C. Valenzuela-Malebrán).

https://doi.org/10.1016/j.jsames.2022.103887
Received 4 February 2022; Received in revised form 8 June 2022; Accepted 9 June 2022
Available online 17 June 2022

recall the 2014 M_W 8.1 Iquique (Hayes et al., 2014; Schurr et al., 2014; Cesca et al., 2016), 2007 M_W 7.7 Tocopilla (Delouis et al.,2009; Schurr et al., 2012), 1995 M_W 8.1 Antofagasta (Ruegg et al., 1996; Delouis et al., 1997) earthquakes and a mega-earthquake in northern Chile in 1877, with estimated M_W 8.8 magnitude (Comte and Pardo, 1991). A second band of earthquakes, at intermediate depths between 80 and 120 km, extends N–S, subparallel to the plate margin, ~220–380 km east of the trench (Sippl et al., 2018); seismicity in this depth band is typically attributed to dehydration processes of mantle lithospheric serpentinite within the downgoing plate (Sippl et al., 2018). A third band of seismicity has been observed further to the east, with depths larger than 180 km. Differently from shallow and intermediate depth seismicity, deeper seismic processes mostly occur within a limited range of latitudes and the physical mechanisms responsible for this seismicity have not been well understood. This seismicity band appears to be segmented from North to South, parallel to the trench, locally clustering at different spots. In particular, a large cluster of seismicity, which we will refer to as the Jujuy cluster, is observed at Lat ~24°S Lon ~67°W (Fig. 1), beneath the Puna-Altiplano plateau. It has been hypothesized that this cluster could be a seismic nest (Zarifi and Havskov, 2003).

Seismic nests are compact seismogenic volumes of the earth characterized by a high stationary seismic activity relative to their surroundings. Seismic nests are continuously active, with the earthquake hypocenters being confined within a small volume so that the seismic activity within such volume is substantially larger than in the surrounding areas (Zarifi et al., 2007). Two classes of intermediate deep nests have been defined (Zarifi and Havskov, 2003); those related to tectonic processes in subduction zones and those located on downgoing slabs and related to dehydration processes and in broader sense to magmatic activity. The three best known tectonic nests are, the Bucaramanga nest, Colombia at Lat 6.8° N, Lon 73.1° W, centered at ~160 km depth (Tryggvason and Lawson, 1970; Schneider et al., 1987), the Vrancea nest, Romania, at Lat 45.7°N, Lon 26.5° E, reaching depths between 70 and 180 km (Carbunar and Radulian, 2011), and the Hindu Kush nest, Afghanistan, where earthquakes tend to occur in form of clusters, the majority located at Lat 36.5° N, Lon 71° E down to depths between 170 and 280 km (Frohlich et al., 1995; Poli et al., 2016). Volcanic nests are more abundant and found at intermediate depths (70–160 km) in central America (Carr and Stoiber, 1973), New Zealand (Blot, 1981b), the New Hebrides (Blot, 1981a), and the Aleutian (Engdahl, 1977). These nests may be related to melting near the upper surface of the subducted slabs. A fluid phase, either silicate melts or hydrous fluid released by dehydration of the slab, lowers the strength of the slab and creates an aseismic zone beneath the active volcanoes (Zarifi and Havskov, 2003). Nest of earthquakes can then develop by stress concentration at the margins of the weak, creeping zones. Tectonic seismic nests provide the best scenario to study the physical mechanism responsible for intermediate depth earthquakes. Intermediate depth earthquakes often occur along the subducting lithosphere, they occur at temperatures and pressures above the point where ordinary fractures

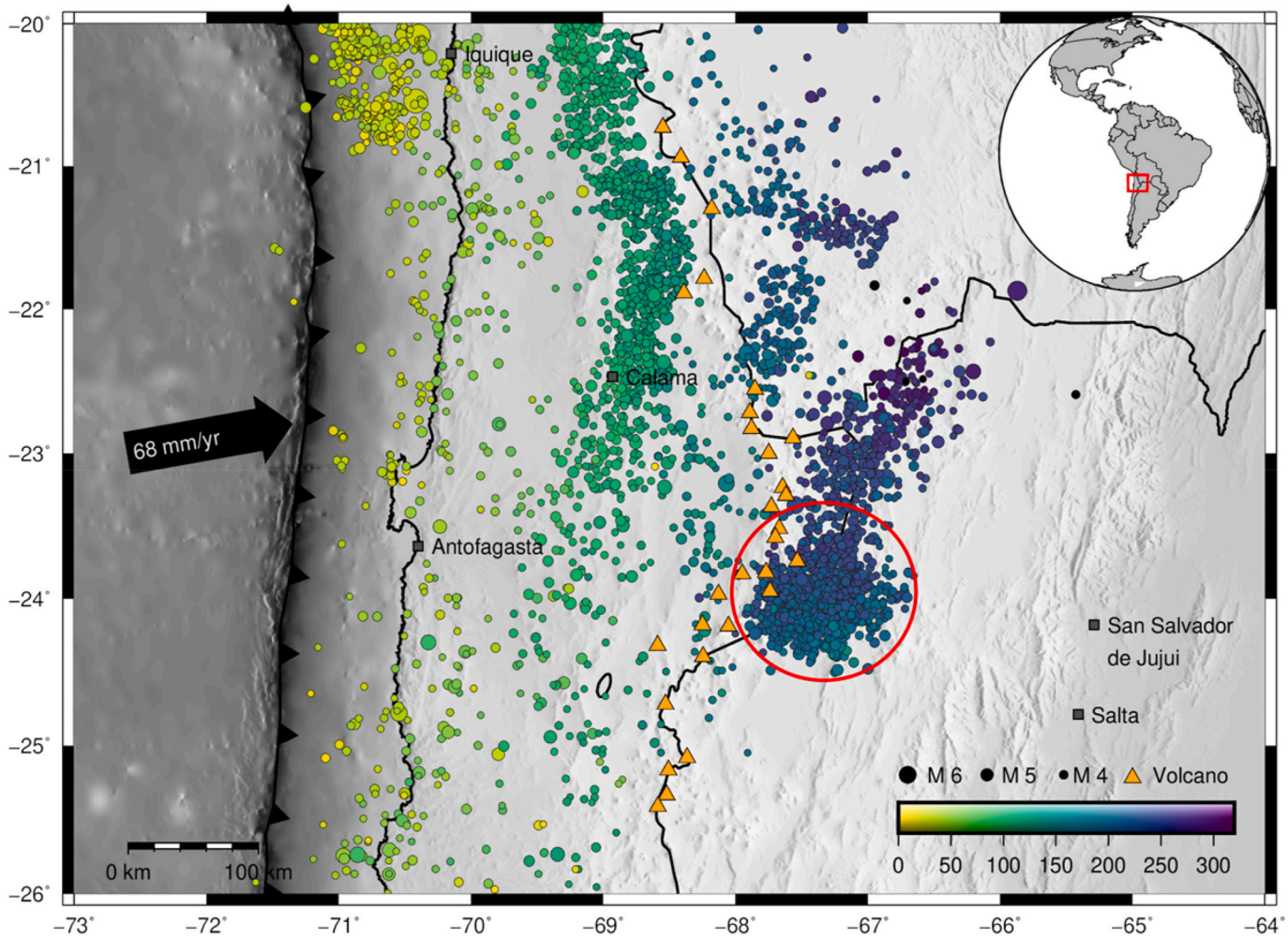

Fig. 1. Map showing seismicity (circles) in the study area between 2010 and 2020 (CSN catalog – National Seismological center of the Universidad de Chile, magnitudes $M_L > 4$). The color indicates the hypocentral depth, the circle size is proportional to the magnitude. Orange triangles denote the locations of active volcanoes. The red circle indicates the location of the Jujuy cluster.

ought to occur, but the physical mechanism responsible for promoting brittle faults is not well constrained and remains uncertain. The three main mechanisms proposed for intermediate depth earthquakes are (i) dehydration embrittlement (Frohlich, 1989; Jung et al., 2004; Hasegawa and Nakajima, 2017), in which hydrated minerals release fluids at particular pressures and temperatures allowing brittle failure to occur, (ii) uncontrolled thermal shear instability (Frohlich, 2006; John et al., 2009; Hasegawa and Nakajima, 2017), which would occur through positive, rapid feedback between shear strain localization and thermal heating, and (iii) mineral phase transformation (Kirby et al., 1991).

The definition of what an earthquake nest represents is somewhat rather qualitative (Prieto et al., 2012). Zarifi and Havskov (2003) suggested that a seismic nest is defined by stationary seismicity within a volume that is substantially more active than its surroundings. Nests differ from aftershock sequences because they have a high rate of persistent activity, whereas a sequence of aftershocks has a high rate of activity after the mainshock, but disappears over a period of time (Utsu et al., 1995; Pavlis and Das, 2000). Nests are distinct from earthquake swarms because swarms are limited in time; earthquake nests, on the other hand, persist (at least) over decades. In conclusion, we use three conditions to define a seismogenic region as a seismic nest: (1) intermediate-depth seismicity, (2) compact seismogenic volume, isolated from nearby activity, and (3) steady activity over time, not following mainshock-aftershock sequences or swarm temporal patterns. Studying the source mechanisms of earthquakes from a seismic nest may provide a clue to further elucidate the processes leading to the occurrence of seismic nests.

This paper has two aims. First, we wish to prove that the seismicity at Lat 22°–25° S Lon 69° to 65° W does accomplish the conditions of a seismic nest, by recollecting more than 40 years of data from different seismic catalogs. Furthermore, we aim to investigate in detail the seismic source processes occurring at this seismogenic spot, specifically by means of hypocentral location, moment tensor inversion, and finite source analysis for the occurrence of large earthquakes in the study region. The careful investigation of this seismic cluster enables us to infer information with unprecedented detail on ongoing seismic processes and to discuss spatial and temporal seismicity patterns in comparison to known nests.

2. Data

We focus on the region spanning Lat 22-25° S and Lon 65-69° W,

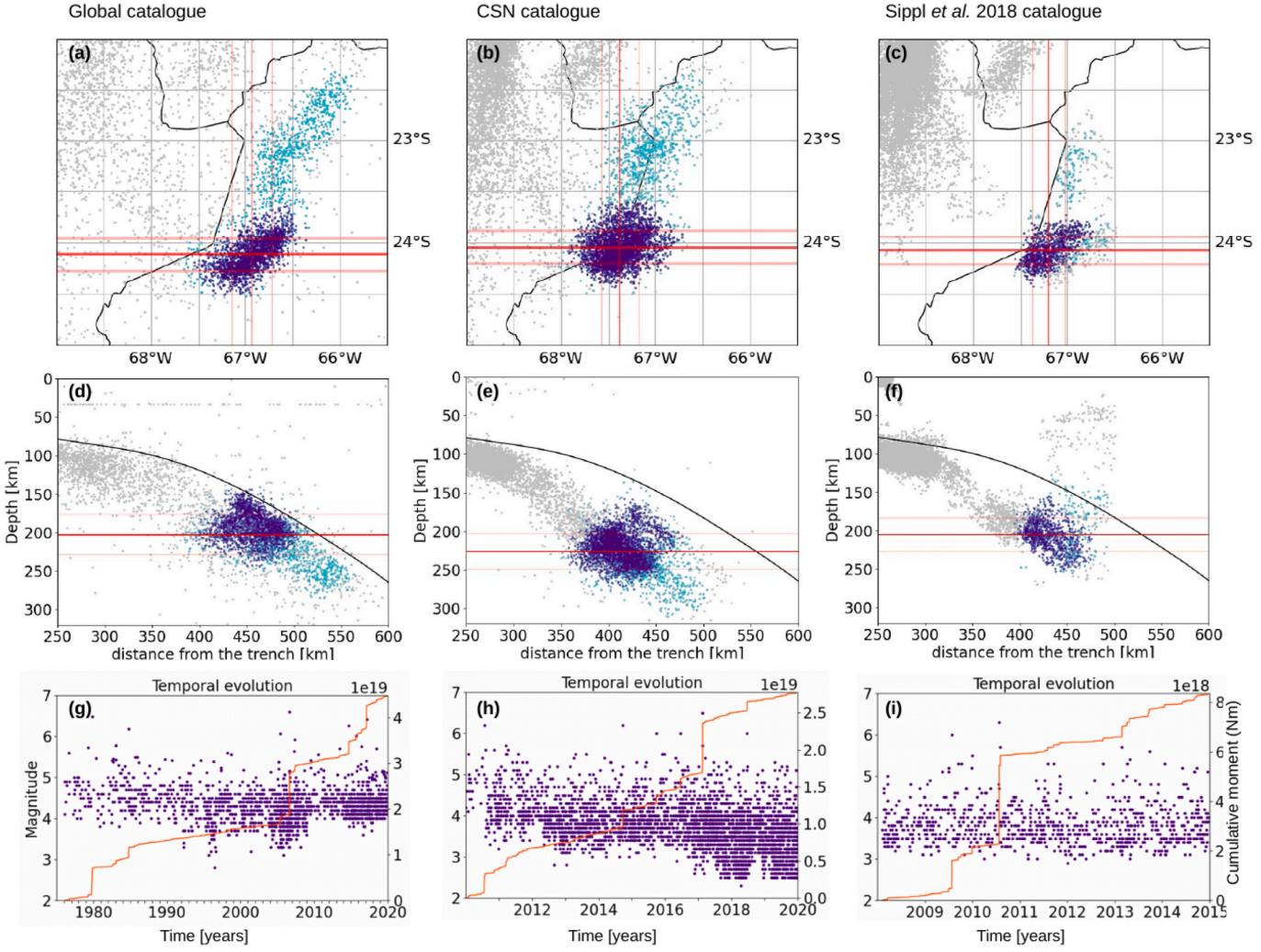

Fig. 2. Results of spatial clustering using the Seiscloud software (Cesca, 2020) applied to the Global catalog (left), the CSN catalog (middle) and the catalog by Sippl. et al. (2018) (right). Panels a–c show the location of the cluster in map view: indigo dots denote to clustered events with clustering parameter $\varepsilon = 0.015$ and Nmin = 30, turquoise dots with $\varepsilon = 0.025$ and Nmin = 50, gray points correspond to unclustered events. Red lines denote mean latitude and longitude, while confidence intervals (1 standard deviation) are plotted in light red. Panels (d–f) show the corresponding seismicity projected along a vertical EW cross-section, red and light red lines denoting average depth and its confidence interval, the black line indicate the slab2.0 (Hayes et al., 2018). Panels (g–i) show the magnitude as a function of time, with the red line indicating the cumulative moment rate only for clustered events (Note different axes in panels g–i).

considering only intermediate-depth events with depths of 150–350 km, which in this region reduces the dataset mostly to intraslab earthquakes. We consider three seismic catalogs (Fig. 2), each with different characteristics. The first one is the seismic catalog of the National Seismological Center (CSN) of the Universidad de Chile, which covers the time period January 1, 2010–December 31, 2019 (http://evtdb.csn.uchile.cl/, last accessed March 2020). The second one is built upon global catalogs, merging Global CMT, GEOFON, and USGS catalogs to produce an extensive earthquake catalog of more than 40 years, from 1973 to 2020, but limited to largest events, mostly above magnitude M_W ~4.5. The third one is an accurate relocated catalog (Sippl et al., 2018) for Northern Chile, based on the regional densification granted by the Integrated Plate Boundary Observatory Chile (IPOC) initiative (GFZ German Research Centre for Geosciences & Institut des Sciences de l'Univers-Center National de la Recherche CNRS-INSU, 2006), but only spanning the time period between 2007 and 2014. The three catalogs provide different contributions. The CSN catalog contains events down to relatively low magnitudes (typically above M 3.0), relying mostly on Chilean stations, so that the location accuracy decreases towards Argentina. The global catalog covers the largest time span and partially provides moment tensor solutions, but only includes the largest earthquakes. The last catalog (Sippl et al., 2018) is the most homogeneous in time and has presumably the highest relative location accuracy, but only covers a time period of 7 years. Our target region is close to the edge of the catalog by Sippl et al. (2018), where the location accuracy decreases. The two local catalogs (CSN and Sippl et al., 2018) have been generated using local networks, with seismic stations which are mostly located to the west of the cluster (i.e. in Chile), which could potentially bias the locations of earthquakes in the deep cluster (beneath the Chile-Argentina border).

For the characterization of the earthquake source processes, we first collected waveforms of the largest earthquakes ($M_W > 6.0$) during the period between 2010 and 2020. Data and metadata pertaining to regional broadband stations were accessed using IRIS and GEOFON FDSN web services. Data was collected for stations with epicentral distances up to 1000 km to perform moment tensor inversion and rupture directivity analysis. The best seismic monitoring configuration, was provided by the simultaneous deployment of permanent and temporal stations, such as from the STRATEGy (Seismic neTwoRk/Array in norThwEstern arGentina) network, that was operational with 13 LE3D-5s three-components sensors in the time period from June 1, 2016 to August 1, 2017 (Zeckra et al., 2016). Consequently, we additionally collected waveform data for earthquakes with magnitudes $M_W > 5.0$ in this time period. In this way, we can expand the azimuthal coverage to the east, and investigate seismic source processes for weaker events.

3. Methods

3.1. Seismicity patterns

For the analysis of seismicity patterns and the assessment of the seismic nest properties, we used clustering tools for seismological applications and a range of statistical seismology analyses. We used Seiscloud, a density-based clustering algorithm (Cesca, 2020) to detect spatial clusters from different seismic catalogs. This method scans the hypocentral distribution of the catalog, searching for regions with high earthquake density to detect seismicity clusters. The spatial boundaries of each cluster are defined according to a pre-set earthquake density threshold. A density based algorithm is suited to identify the spatial properties of a seismic nest, for which a drop in hypocenter density is expected outside the compact volume of the nest. Seiscloud treats potentially isolated earthquakes and those located in regions of low seismicity as non-clustered seismicity. For the spatial clustering, we use the Euclidean distance between hypocenters as a metric. For this study, we tested the clustering parameters in the range Nmin = 30–50 and ε = 0.015–0.025 km, which imply that an earthquake cluster is formed whenever, for a given earthquake, there are at least 30 to 50 other earthquakes with hypocenters located at less than 15–25 km distance (Cesca, 2020). We have further analyzed the spatial distribution of seismicity in the study area by mapping the epicenter density and the cumulative Benioff strain (Benioff, 1951), discretizing the study region using a regular grid with 0.05° × 0.05° spacing. The Benioff strain is defined as the square root of the radiated seismic energy (SE) and proportional to the elastic strain released by an earthquake. The cumulative seismic energy for each grid point is further estimated from the seismic catalogs, either based on moment magnitudes or local magnitudes, in both cases relying on the Hanks and Kanamori (1979) relations. In order to investigate seismicity rate variations within the cluster, we study the distribution of interevent times, i.e. the times between two consecutive earthquakes.

3.2. Seismic sources processes

The second set of methodologies is devoted to investigating seismic source processes for individual, large earthquakes. To perform the moment tensor (MT) inversion we used the open source Grond software (Heimann et al., 2018). The MT inversion is based on broadband seismic data at regional to teleseismic distances. Displacement waveforms are filtered in the frequency band 0.06–0.15 Hz for magnitudes 5.0–5.9 and 0.04–0.09 Hz for magnitudes 6.0–6.4, tapered to extract P waveforms on vertical components and S waveforms on transversal and radial components and downsampled to 2 Hz. We considered seismic stations at an epicentral distance of 150–1000 km for the largest events and 150–600 km for the events with magnitudes below M 6.0. Precalculated Green's function databases are used for computing synthetic seismograms, assuming a regional 1-D velocity model from the CRUST2.0 database (Bassin et al., 2000). Waveform data is fitted in the time and frequency domain, by simultaneously adjusting displacements waveforms and their amplitude spectra. The MT inversion provides the moment tensor components, centroid location, centroid time, and earthquake duration. We perform full moment tensor inversion, to better discuss potential non-double-couple terms: the full moment tensor is decomposed as the sum of an isotropic term, which corresponds to a volume variation at the focal region, and a deviatoric one, which is further decomposed as the sum of a double couple (DC) and a compensate linear vector dipole (CLVD) (Jost and Hermann, 1989).

3.3. Directivity method

The identification of directivity effects, describing the directional mode of rupture propagation, can provide us relevant information to understand the earthquake source processes of the largest earthquakes. Rupture directivity analysis allows reconstructing the fault geometry and resolving the fault plane ambiguity. Unilateral ruptures, as well as symmetric and asymmetric bilateral ruptures are modeled based on the apparent duration estimated at different azimuths; e.g. for unilateral ruptures, shorterst apparent durations are found ahead of the rupture direction. We perform the directivity analysis for the largest earthquakes at the Jujuy cluster with a good azimuthal coverage of seismic recordings, selecting six target earthquakes with M_W larger than 5.9 and depths between 150 and 250 km.

The rupture directivity mode and its direction are derived from the azimuthal distribution of apparent source time functions (ASTFs), which reveal the relative moment rate functions as seen at each seismic station. In the case of intermediate and deep-focus earthquakes, the initial portion of observed P-wave displacements is well separated from later seismic phases and provides a reasonable approximation of the source time function with a scalar correction for the seismic moment (Fukao, 1972; Kikuchi and Ishida, 1993; Beck et al., 1995; Tibi et al., 1999), thus eliminating the need for deconvolving structural effect. This approach is applied for our deep target earthquakes where a relatively undistorted approximation of the ASTFs is recovered from the first pulse of the P

displacement waveforms at near-regional distances. We inspect both raw velocity and displacement waveforms to manually pick the P-arrivals, assuming a picking error of 0.05 s. To identify the end of the apparent durations, we use a procedure to automatically pick the first maximum of the so-called slip function, which corresponds to the integration of the P-wave displacements (Fig. S1). This maximum corresponds to the time when the seismic moment is fully released, indicating the end of the apparent durations at each seismic station. We excluded those stations with the lowest signal-to-noise ratio for the P-arrivals, which hamper the recognition of ASTFs and the maximum of the slip function. ASTFs are normalized to unit area according to the total seismic moment of each target earthquake. Finally, the azimuthal variations of the apparent durations are adjusted using unilateral and asymmetric bilateral rupture models (for technical details, see Cesca et al. (2011) and López-Comino et al. (2016)), revealing the preferred rupture directions.

4. Results

4.1. Seismicity patterns

The spatial clustering detects a compact region of high seismicity density beneath the Puna-Altiplano region. The seismic cluster is identified independently of the considered seismic catalog (Table 1, Fig. 2). The cluster has an outstanding density of hypocenters, which substantially drops in all directions in the surrounding region.

The average horizontal location and depth of the cluster (Table 1) shift slightly, depending on the considered catalog. Consistent epicentral locations are found for the CSN and Sippl et al. (2018) catalogs, while they are shifted SE in the global one. Mean hypocentral depths of 192, 207, and 221 km are found for the global, Sippl et al. (2018) and CSN catalog, respectively. All clustering results resolve a similar cluster shape, slightly elongated in the NE-SW direction. At depth, the cluster becomes progressively deeper towards the east, in alignment with the background seismicity and with the slab geometry (SLAB2.0, Hayes et al., 2018). Seismicity and moment rate, considering events with magnitude M 4 or larger, are as high as 107 events/year and 2.7 10^{18} Nm/year, respectively. Higher values estimated with in the CSN catalog are attributed to its lower magnitude of completeness.

Interevent times are estimated based on the two most homogeneous catalogs, by CSN and Sippl et al. (2018). In both cases, independently of the magnitude ranges and different time coverages of the two catalogs, we obtain coefficient of variation (CV) values close to 1, which indicates a Poissonian distribution of occurrence times (Maghsoudi et al., 2014), excluding both the presence of mainshock-aftershocks sequences and short duration seismic swarms, alternating with quiescence periods. The temporal evolution of the moment rates in all catalogs also shows a continuous increase of the cumulative moment over years to decades (Fig. 2g–i), which implies that the seismogenic region was active in a continuous mode over each time period in the different catalogs.

The study of seismicity density and cumulative Benioff strain are shown in Fig. 3. First, the increase in the number of earthquakes within an oblique band with the NNE-SSW direction is highlighted for all catalogs considered, identifying the main cluster and the higher density of seismicity in the southern part of it, and thus corroborating its identification with the density-based clustering algorithm. The clustering results obtained using both the catalogs CSN and Sippl et al. (2018) further identify a bimodal distribution, with two sub-volumes of enhanced hypocentral density and moment release within the main cluster (Fig. 3e,f, Fig S2). This seems to be a true feature of the seismicity, considering that the two catalogues are produced using different data and methods.

4.2. Source processes

We perform the MT inversion to investigate in detail seismogenic processes within the seismic nest. We resolve source parameters for largest earthquakes only (M > 6.0) in the period between the years 2010–2021, further including weaker earthquakes with M > 5.0 during the period June 2016–August 2017, taking advantage of temporal seismic installations in Argentina (Krüger et al., 2016), which reduce the azimuthal gap to the East. We obtained full MT solutions for 10 earthquakes (Fig. 4, Tab. S1 and later in Fig. 6). Focal mechanisms are predominantly striking NS, with one plane sub-vertical and one sub-horizontal. The orientations of the P axis ranges from sub-vertical to ~45° plunge westward, and the T axis from sub-horizontal to ~45° plunge eastward. For "vertical mechanisms" (i.e. P and T axes plunges of ~45°), tiny rotations around the sub-horizontal null axis result in normal faulting or thrust faulting components. The majority of our solutions present a normal faulting component, while 3 events, located at the NW of the nest, show a thrust faulting component. Fig. 6d shows resolved non-DC (CLVD and isotropic) components using the Hudson representation. CLVD estimates are sometimes large and scattered, including positive and negative values, and in general, poorly resolved. The isotropic components, however, have a smaller scatter and indicate positive components between 5% and 30% for all analyzed events.

Our centroid locations are in best agreement with hypocentral locations in the Sippl et al. (2018) catalog (Fig. S3). The centroid depths range from 150 to 250 km, becoming progressively deeper towards the east, in alignment with the slab direction. According to our results, most events occurs in the subducted plate. Moment tensor solutions are in general agreement with Global CMT solutions, when available.

4.3. Rupture directivity analysis

A similar azimuthal variation pattern of apparent durations is observed for the six selected target earthquakes. The shortest apparent durations of the source time function (ASTF) are identified at W to NW azimuths and the largest durations at the opposite directions. Apparent durations range from 2.4 up to 10.2 s (Fig. 5). These results reveal a common unilateral rupture pattern with preferred rupture propagation toward an azimuth of 276°–320°, and average rupture times ranging among the events from 4.3 s to 7.8 s, increasing with the earthquake magnitude (Tab. S1). The sub-vertical nodal plane oriented NS, which was identified from the focal mechanisms, has to be discarded as possible rupture plane, since the rupture directivity analysis reveals a westward, lateral rupture propagation. This result suggests that the rupture occur for all earthquakes along the other sub-horizontal plane. The fault plane identification is more questionable for the M_W 6.25 November 30th, 2020 earthquake, where the two planes have a similar dip angle.

Earthquake source complexities can be also discussed from the shape

Table 1
Overview of the spatial seismic clustering results based on three considered catalogs. The table reports catalog name, number of clustered events, minimum and maximum magnitude within the cluster, average depths, latitude and longitude, seismicity rate, and moment rate of the cluster. (*values calculated during the period between 2010 and 2020).

Catalog	Cluster Size	M_{min}	M_{max}	Depth [km]	Lat S	Lon W	Seismicity rate M > 4 [N/yrs]	Moment rate M > 4 [10^{18}Nm/yrs]
CSN	3146	2.3	6.5	221	24.035	67.393	107	2.7
Sippl	877	2.9	6.3	207	24.097	67.245	40	1.2
Global	1950	2.8	6.6	192	24.097	66.925	61*	1.5*

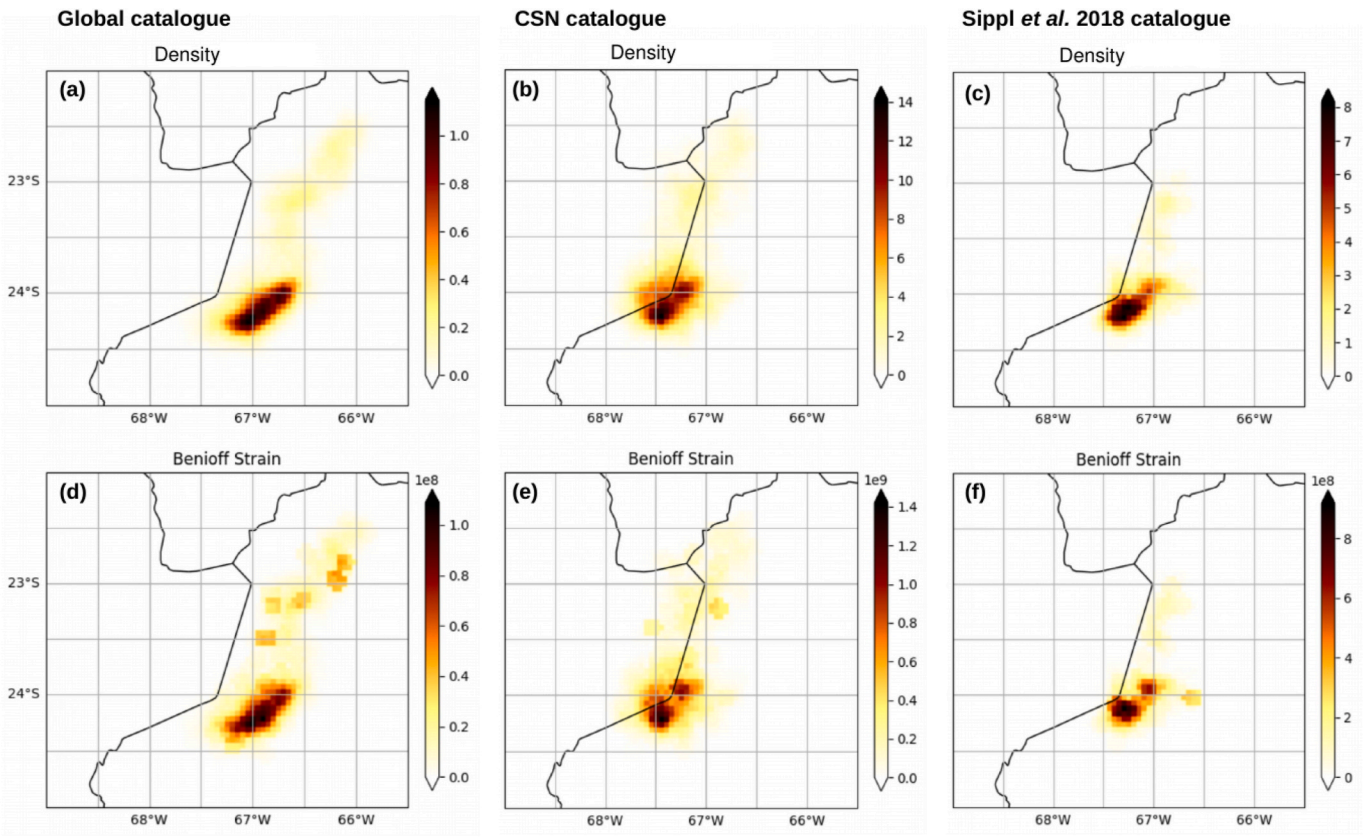

Fig. 3. Maps of seismicity density = number per cells of 10 km radius (panels a–c) and cumulative Benioff strain (panels d–f), based on the three seismic catalogs: Global catalog (left), CSN catalog (middle) and Sippl.et al. (2018) catalog (right). The images are produced assuming a grid of 0.05°, reporting values for cells of 10 km radius. The dark region at the Chilean-Argentinian boundary denotes the high density Jujuy cluster.

of the ASTFs. Two pulses are clearly visible for the M_W 6.34 February 18th, 2017 and M_W 6.12 August 4th, 2016, earthquakes, which reveal the complex rupture of at least two asperities. On the other hand, the remaining events show one single pulse revealing simple earthquake ruptures. We note that the M_W 6.25 November 30th, 2020 earthquake reveals a slight asymmetry of the seismic moment release towards the end of the rupture process.

5. Discussion

5.1. The Jujuy cluster as a seismic nest

The Jujuy cluster, already mentioned in previous studies (Zarifi and Havskov, 2003; Prieto et al., 2012), is here studied accurately for the first time. Zarifi and Havskov (2003) first suggested that this cluster could be a seismic nest, but did not provide a clear evidence. Indeed the Jujuy seismic nest exhibits a particular type of intermediate depth seismicity, that clusters with a high rate of activity, outstanding in terms of rate and moment release with respect to the neighbouring region, and with seismic activity observed over decades. Considering hypocentral and centroids locations, the Jujuy Nest at depths of ~200 km, appears to occur within the subducting oceanic plate.

On the basis of the analysis of an extended seismicity catalog, we can confirm that the Jujuy cluster is a seismic nest, as the three conditions posed in the introduction have been met (Zarifi and Havskov, 2003). The first condition is obvious, given the intermediate depth of the Jujuy cluster. The second condition of a compact, isolated seismogenic volume is confirmed by the spatial clustering results, which identify a volume of high seismicity density, surrounded by region of lower activity. The spatial cluster is identified independently using three different catalogs (Fig. 2d–f). The third condition is confirmed by the temporal evolution of magnitudes and moment release within the detected cluster, which is continuous over decades (Fig. 2g,h,i), and by the estimated coefficient of variation (~1.0), which excludes the presence of swarm and/or mainshock-aftershock sequences. In the light of the classification of seismic nests (Zarifi and Havskov, 2003), the Jujuy nest is not only closely related to tectonic processes in subduction zones, but also to volcanism. An indication for the latter is the attenuation tomography (Schurr et al., 2003) revealing that mantle melts produced by dehydration processes at the Jujuy nest feed the largest Quaternay backarc volcano in the overlaying Puna altiplano.

5.2. Seismogenic processes at the jujuy nest

Centroid location poses the nest within the oceanic plate; their distribution of hypocenters becomes progressively deeper towards the east, aligning with the slab geometry (Hayes et al., 2018). The results from the focal mechanisms are consistent with the slab's subduction stress regime. Slab pull is an expected driver for seismicity at these depths (Lemoine et al., 2002; Contreras-Reyes and Osses, 2010). The focal mechanisms for all 9 events (Fig. 6) show overall vertical dip-slip mechanisms to normal faulting. The rupture directivity analysis resolves failure of subhorizontal to westward dipping low-angle faulting, almost perpendicular to the slab plunge. The slab curvature, progressively steepening above this depth can play an important role in generating high stress gradients and controlling water migration paths, which may support this type of failure within the slab.

Considerable non-DC components are resolved for most studied earthquakes. While the scatter of CLVD components prevents any robust interpretation of these terms, similar, positive isotropic components are resolved for most events. The positive isotropic component is typically below 30%. A positive isotropic source component, implying volumetric

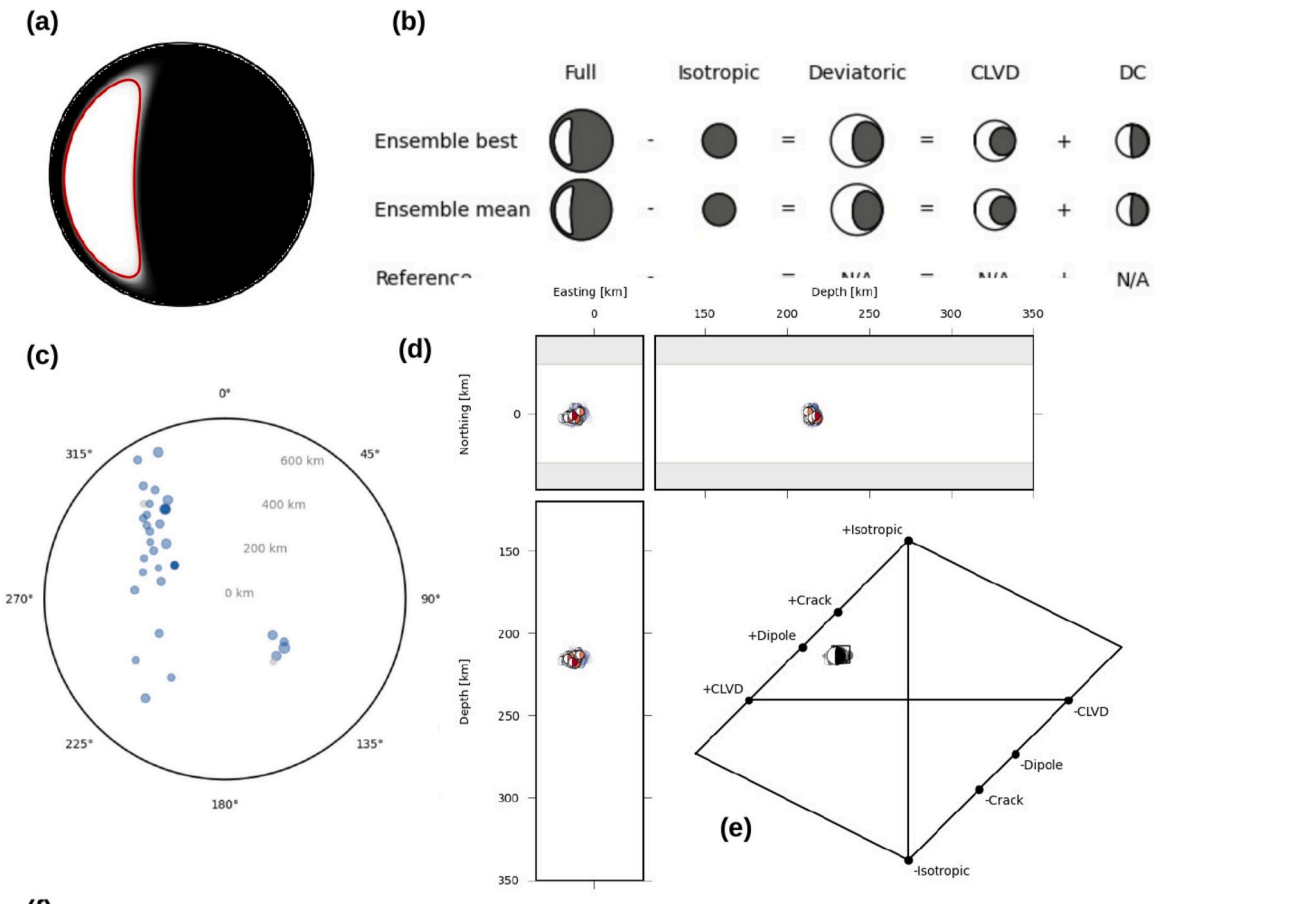

(f)

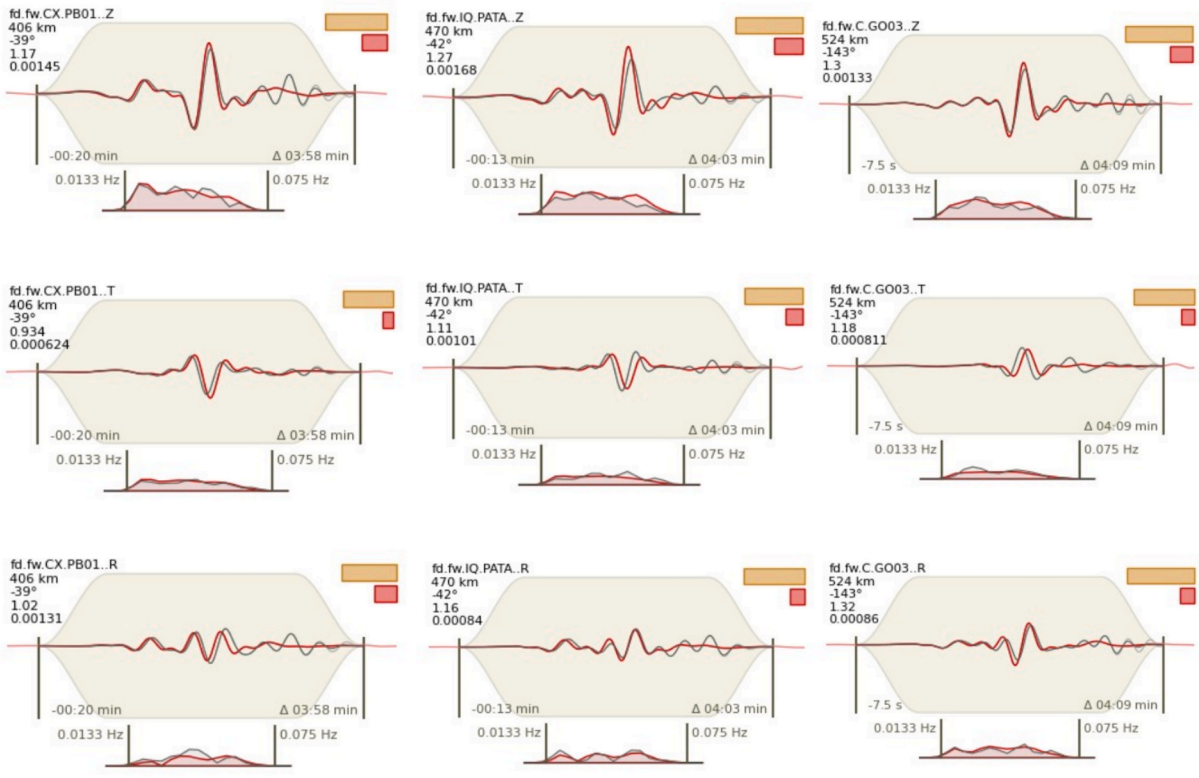

(caption on next page)

Fig. 4. Example of the moment tensor inversion result, earthquake date February 18, 2017, M_W 6.3. (a) Fuzzy beachball illustrating the MT solution uncertainty. (b) Decomposition of the best MT solution into isotropic DC and CLVD component. (c) Station distribution around the epicenter. (d) Resolution of the centroid depth, easting and northing relative to the starting position, showing the ensemble of solutions resulting by boostrap (map view and cross sections have the same scale). (e) Hudson plot showing non-DC components of the event (the ensemble of solutions is compact, denoting quite small uncertainties). (f) Examples of waveform and spectral fits at three stations and three components (top left labels report station and channel name, epicental distance, azimuth, target weight and target misfit. Colored boxes on the upper right show the relative weight of the target and the relative misfit contribution). Red and black lines indicate synthetic and recorded waveform data, respectively. The beige shaded area represents the time window and taper function. Station name, azimuth and distance to the epicenter are indicated above each column. Numbers within the panels describe the time window and frequency band.

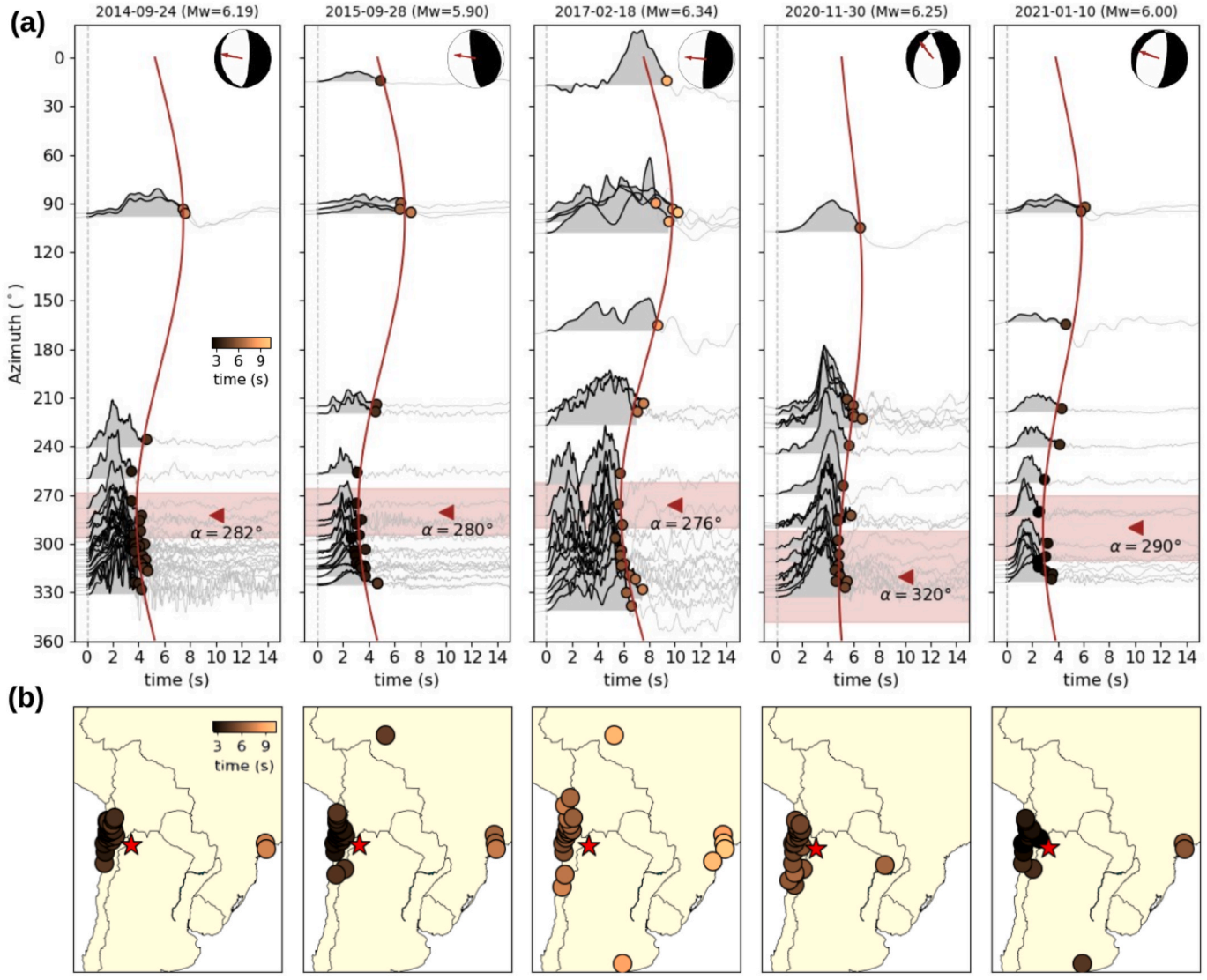

Fig. 5. Rupture directivity inferred by the Apparent Source Time Functions (ASTFs) for five selected target events at the Jujuy cluster. (a) ASTFs (black lines) are obtained from the observed P-wave displacements (gray lines) and normalized to unit area according to the total seismic moment (gray area) of each target event (see top label in each plot). Traces are aligned along the first P onset at zero time and plotted according to station azimuth. Theoretical predictions for the inverted unilateral models (brown lines) are shown revealing the directions (brown triangles) and their uncertainties (brown areas) of the predicted rupture directivities (α). (b) Map of near-regional seismic stations used (circles) showing the apparent durations (color bar) and the epicenter of each target event (red star). Red arrows in the beachballs of panel denote the directivity.

increase has been resolved for shallow earthquakes within volcanic and mining environments, accompanying e.g. explosions processes, magmatic intrusions (e.g. Dahm and Brandsdottir, 1997), and tensile cracks (Vavryčuk, 2015). In our case, it may reflect specific source processes or geometries. One of the most invoked seismogenic processes at intermediate depths is dehydration embrittlement (Hacker et al., 2003; Jung et al., 2004). In this process, the dehydration of serpentines results in the generation of fluid volumes that increase the pore pressure, reduce the effective stress, and finally allow brittle failure to occur at depth. While dehydration reactions are accompanied by a decrease in solid volume, it also produces substantial fluid volumes (e.g. Jung et al., 2004; Brantut et al., 2017), so that brittle failure could include opening tensile failures and thus explain the resolved isotropic components.

5.3. Comparison with other nests

We compare here the Jujuy nest with other known seismic nests (Table 2). The Jujuy nest extends laterally with an area of approximately

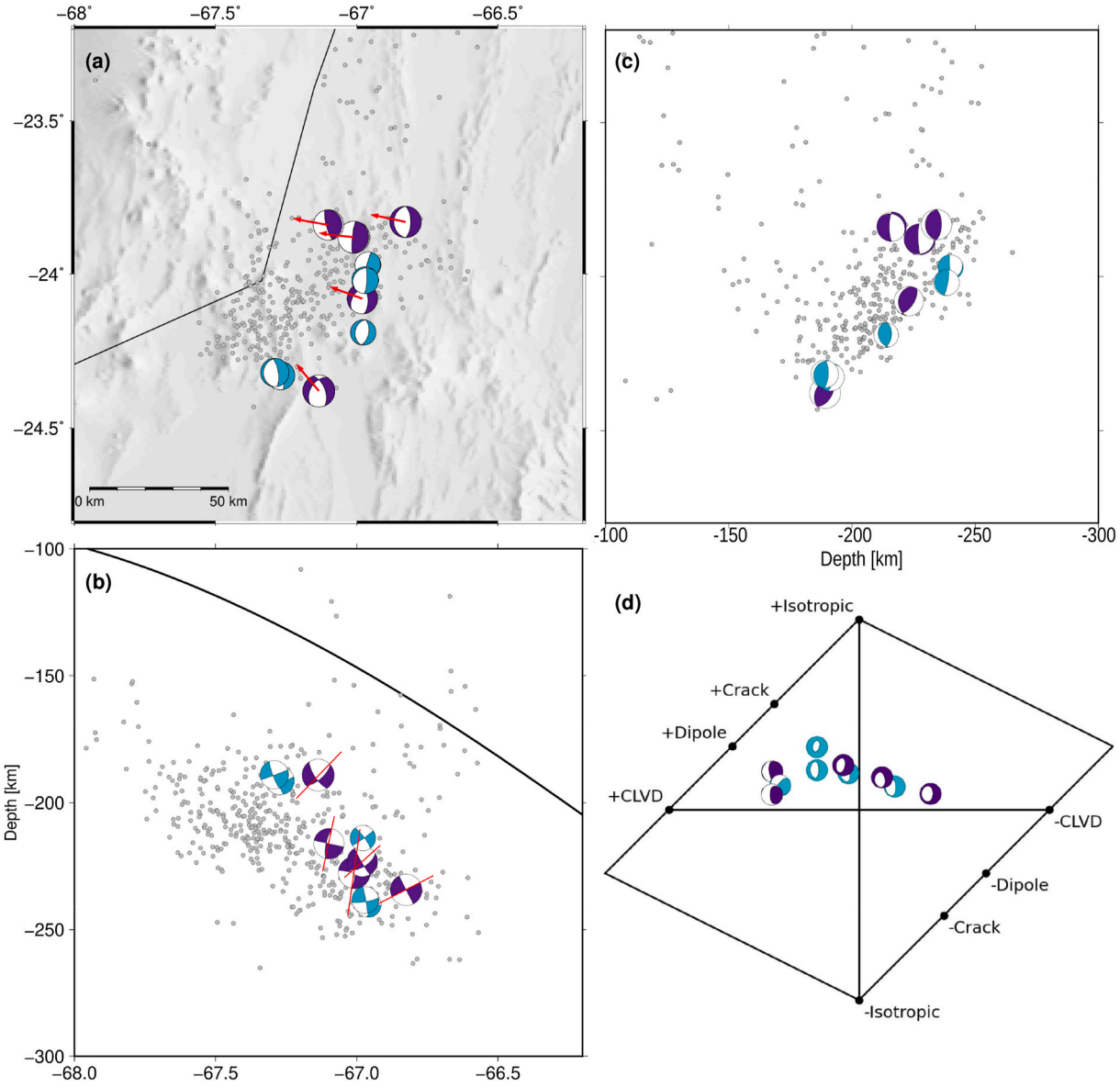

Fig. 6. Moment tensor inversion results for the events during the period 2010–2021 $M_W > 6.0$ (indigo) and the period 2016–2017 $5.0 < M_W < 6.0$ (turquoise) (a) focal mechanisms in the map, the red arrows indicate the results of the directivity, gray dots denote the seismicity retrieved from (Sippl2018a) catalogue. (b) Cross section in the latitude −24°, gray dots denote the seismicity retrieved from Sippl. et al. (2008) catalogue, red lines denote the estimated rupture length. (c) Cross section in N–S at longitude −67°. (d) Hudson plot showing non-DC components of the best-fitting solutions of individual events results.

Table 2
Comparison of some observed features of the three most important seismic nests after Prieto et al. (2012) and the Jujuy nest, as resolved in this study.

Nest:	Hindu Kush	Vrancea	Bucaramanga	Jujuy
Mean location (lat, lon)	36.5°N, 71.0°E	45.7°N, 26.5°E	6.8°N, 73.1°W	24.1°S, 66.9°W
Depth range (km)	175–250	70–180	145–165	150–250
#events M > 4 (years^{-1})	55 (ISC)	5 (ISC)	15 (ISC)	106 (CSN)
Focal mechanism	Vertical T-axes Variable P-axes	Vertical T-axes Horiz. P-axes	Highly variable East dipping T-axes	Steep P-axes
Mag max (Mw G-CMT)	6.6 (July 14, 1991)	7.5 (March 4, 1977)	5.4 (February 17, 2008)	6.6 (August 25, 2006)

70 × 50 km at a depth between 150 and 250 km, associated with intermediate depth earthquakes that occur at convergent plate boundaries within the subducting lithosphere. It is a highly relevant nest because it has substantially higher seismicity rate, compared with other nests, it has 609 events with magnitude larger than M_W 4 over 10 years, including 6 events of magnitude larger than M_W 6, which is about twice as high as the Hindu Kush nest, which was considered the most active nest on earth. We did not find repeating earthquakes in this study but a high similarity among focal mechanisms. Sub-horizontal fault planes have been observed at other nests, for example at the Bucaramanga and Hindu Kush nests. The density of hypocenters at the Jujuy Nest is lower than at Bucaramanga, the nest with the highest recorded density. The Jujuy nest shows a bimodal distribution of high-density seismicity volumes, a feature which is also found at the Hindu Kush Nest. Other similarities with the Hindu Kush nest concern the depth and magnitude range. A final similarity concern the location beneath high topography regions: the Hindu Kush nest is located in a subduction zone associated with the collision of the Indian and Eurasian plates (Pregler and Das,

1998; Lister et al., 2008) beneath one of the highest topography areas of the Tibetan plateau, while the Jujuy nest is located below the Puna plateau along the Andes.

5.4. Structural properties at the jujuy nest

It has been shown that the subduction of ridges can alter the distribution of seismiciy along the slab (Yáñez et al., 2001). For example, the subduction of the Juan Fernandez ridge between 30° and 34° Lat S affects the seismicity rate and spatial distribution of intermediate and deep focus earthquakes. At intermediate depths the seismicity rate is much lower along the path of the subducting ridge, while it is clustering at its sides (Gao et al., 2021b). Something similar may also happen at the Jujuy cluster, which location is adjacent the modeled subduction of the

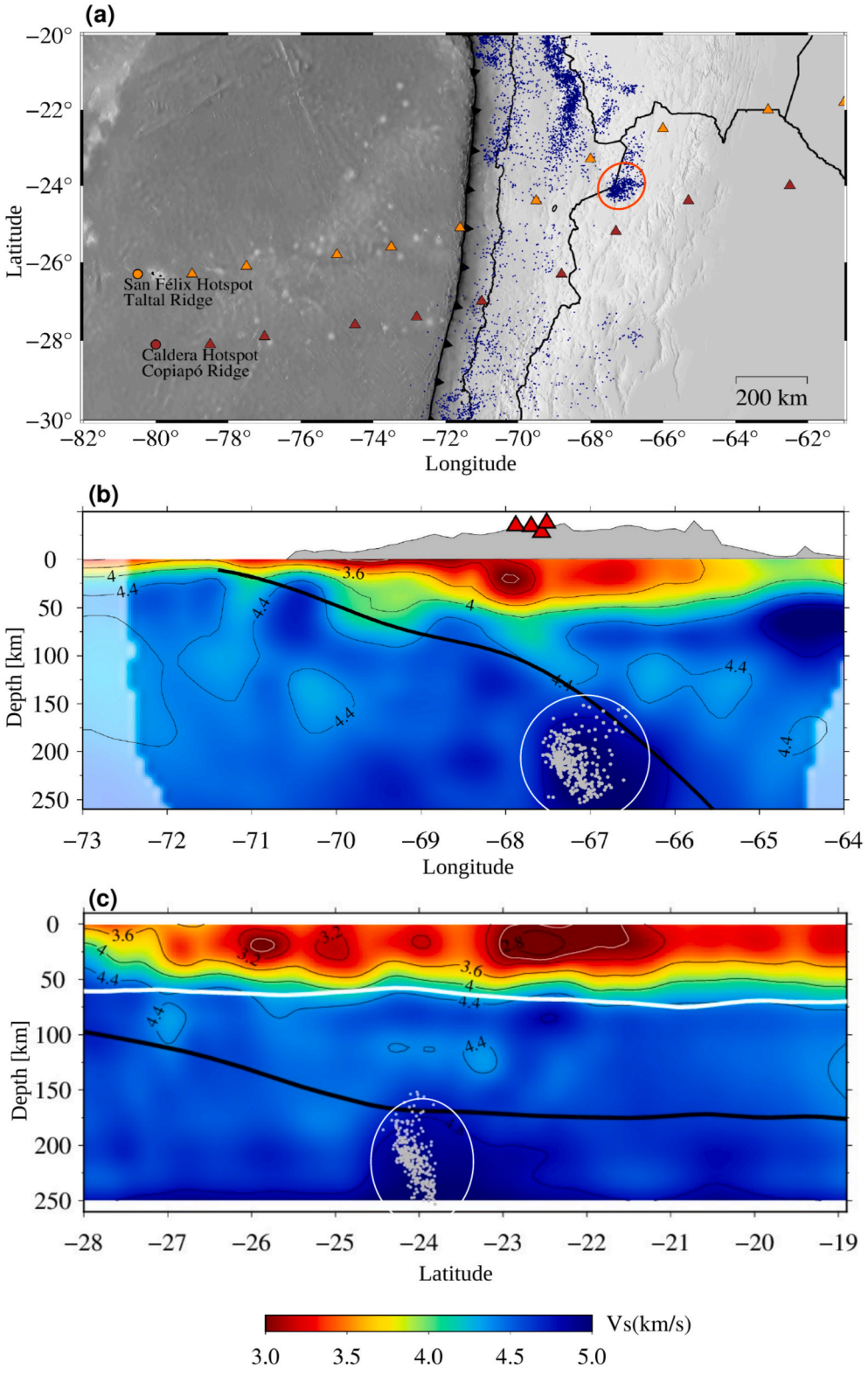

Fig. 7. Correlation among the location of the Jujuy nest, the predicted path of subducted ridges (after Bello-González et al., 2018 and tomography (after Gao et al., 2021a) (a) The map shows regional seismicity (Sippl et al., 2018) above magnitude M 4 (dark blue points) and the predicted path of Taltal Ridge (orange triangles) and the Copiapó Ridge (brown triangles), after Bello-González et al. (2018). (b–c) E-W and N–S cross-sections of the S wave velocity distribution (after Gao et al., 2021a). Reference latitude of panel b is 24° Lat S, reference longitude of panel c is 67° Lon W. In both plots a black line denotes the slab2.0 geometry (Hayes et al., 2018), the white line in plot c denotes the Moho, gray dots are the earthquake hypocenters at the Jujuy nest and a white circle the rough position of the Jujuy nest. The location of volcanoes is shown in panel (b), denoted by red triangles.

Taltal ridge and Caldera ridge shown in Fig. 7a (Bello-González et al., 2018). Another close example is the Pucallpa Nest, located in eastern central Peru, the nest and associated Mendaña fracture zone appears to define the northern margin of a sag in the Peruvian flat slab related with the Nazca Ridge (Wagner and Okal, 2019), but the causes of flat slab nests and the role they play in the spatio-temporal evolution of slab geometry is still not fully understood. At the same time, recent seismic tomographic results ((Gao et al., 2021a) based on multi-scale full seismic waveform inversion showed the presence of a high Vs velocity anomaly (Fig. 7b–c), extending from ~150 km to more than 300 km depth at ~ Lat 24° S, Lon 67° W, thus roughly matching the location and extent of the Jujuy nest. It can be observed in the N–S cross section of the tomography that this anomaly occurs in a narrow latitude band, at ~24° Lat S. Although the tomographic resolution may be relatively low at this depths, the seismicity appears to be confined within the volume of high velocities, suggesting that there the conditions for brittle failure are met. Conversely, lower velocities imaged by the tomography towards the South and North (Gao et al., 2021a) would correspond to different rheological conditions, preventing the seismicity to extend further in latitude. Other regional high-velocity anomalies are also accompanied by seismicity: for example, another high-velocity anomaly at 22–23° Lat S on the tomoghaphy coincides with an intermediate depth seismic cluster previously studied by Sippl et al. (2018) and Contreras-Reyes et al. (2021), which has been attributed to dehydration of lithospheric serpentinite. Evidence for the presence of rising fluids and melts from the subduced oceanic lithosphere above the Jujuy nest and towards the overlying mantle wedge has been provided by attenuation tomography (Schurr et al., 2003). This suggests the seismic nest as the source of these fluids, supporting again that high dehydration of minerals takes place at the nest and dehydration embrittlement as the first cause of seismicity there.

The directivity results resolve a sub-horizontal rupture plane for all studied earthquakes, in general slightly dipping Westwards (i.e. opposite to the slab plunge). We also resolve a predominance of pure unilateral ruptures, propagating from East to West. Fault planes are sketched in Fig. 6b, together with the spatial extent of the nest. Given that the nest defines the limited volume where seismicity can occur, it also poses an upper bound to the largest potential rupture. Based on the orientation of the rupture areas and the size of the cluster we estimate that the rupture length shoud not exceed 50 km. We estimate the rupture length of the events for which the directivity analysis was performed, assuming a rupture velocity of 4.0 km/s (~90% of the S wave velocity resolved by Gao et al. (2021a,b) within the nest). We then use our estimates to build an empirical relation among moment magnitude and length, similar as in Wells and Coppersmith (1994):

$$M_W = a + b * \log(\text{rupture length [km]})$$

Where the best fit is found for a = 3.9 ± 0.7 and b = 1.6 ± 0.5. Consequently, the upper limit in the rupture length also corresponds to an upper limit of the moment magnitude at the Jujuy Nest, which we estimate as M_W ~6.7. This value is slightly larger than the known maximum magnitude in the nest (M_W 6.6, August 08, 2006).

6. Conclusion

Given the intermediate depth of the seismicity of the Jujuy cluster, the compact, isolated seismogenic volume and seismic activity observed for decades, we confirm that the Jujuy cluster is a seismic nest. It is independently identified by three different catalogs, resolving a similar cluster shape, slightly elongated in the NE-SW direction. This nest is closely related to the tectonic processes in the subduction zones. The location of the centroid of the nest is indicated within the oceanic plate; the nest is increasingly deeper towards the east, aligning with the geometry of the slab. The Jujuy nest has a higher seismicity rate compared to other nests previously studied, with a depth and maximum magnitude similar to the Hindu Kush nest.

We resolve the processes of the rupture, using MT solutions and directivity analysis to describe the cluster with unprecedented details. The results from the focal mechanisms indicate down-east dip tension within the slab. The rupture directivity analysis indicates subhorizontal to westward low-angle dip faulting, almost perpendicular to the slab plunge.

Our interpretation is that seismicity occurs in response to the dehydration of lithospheric serpentinite, which feeds ascending fluids and melts towards the overlying mantle wedge. The specific location of the nest may be controlled by high gradients rates or the fluid channels in the bending section of the slab.

The confined location of the Jujuy nest corresponds to a hagh S wave velocity anomaly within the Nazca plate imaged by tomography (Gao et al., 2021a,b), which indicates that the conditions for brittle failure are only met within such volume and may justify the presence of a nest. The nest location is also adjacent to the interpreted subduction of two ridges, which could favour the occurrence of seismicity at its sides.

The Jujuy Nest produces large earthquakes (the largest known to date is M_W6.6). However, the compact size of the seismogenic volume suggest an upper bound for the maximal magnitude. Based on the resolved nest geometry and faulting geometry of the studied earthquakes, we estimated that the maximal magnitude at Jujuy nest would be M_W ~6.7.

Credit author statement

C. Valenzuela-Malebrán: Writing – original draft, Methodology, Investigation, Formal analysis, Data curation, Conceptualization, Visualization. **S. Cesca:** Writing – review & editing, Supervision, Methodology, Conceptualization. **J.A. López-Comino:** Writing – review & editing, Methodology, Visualization. **M. Zeckra:** Writing – review & editing, Data curation. **F. Krüger:** Writing – review & editing, Data curation. **T. Dahm:** Writing – review & editing, Supervision.

Declaration of competing interest

The authors declare that they have no known competing financial interests or personal relationships that could have appeared to influence the work reported in this paper.

Acknowledgments

CV acknowledges the scholarship granted by the National Commission for Scientific and Technological Research (ANID—Becas Chile, Chile). The seismic catalogue was provided by the Centro Sismológico Nacional (CSN, Chile; http://www.sismologia.cl/, last accessed 2020 March 15), waveforms used pertains to the following networks: Red Sismologica Nacional (RSN), C1 (Universidad de Chile 2012), Chilean National Seismic Network, C (https://www.fdsn.org/networks/detail/C/), Geoscope, G (IPGP 1982) and STRATEGy (Krüger and Hongn, 2016). Seismological data and metadata were accessed through the IRIS and GEOFON web service. J.A.L-C. was financed by the European Union's Horizon 2020 research and innovation program under the Marie Skłodowska-Curie grant agreement 754446 and UGR Research and Knowledge Transfer Found–Athenea3i and the Deutsche Forschungsgemeinschaft (DFG, German Reuter Foundation, Germany) - Projektnummer (407141557).

Appendix A. Supplementary data

Supplementary data to this article can be found online at https://doi.org/10.1016/j.jsames.2022.103887.

References

Angermann, D., Klotz, J., Reigber, C., 1999. Space-geodetic estimation of the nazca-south America euler vector. Earth Planet Sci. Lett. 171 (3), 329–334.

Bassin, C., Laske, G., Masters, G., 2000. The current limits of resolution for surface wave tomography in north America. EOS Trans AGU 81, F897.

Beck, S.L., Silver, P., Wallace, T.C., James, D., 1995. Directivity analysis of the deep Bolivian earthquake of June 9, 1994. Geophys. Res. Lett. 22, 2257–2260. https://doi.org/10.1029/95gl01089.

Bello-González, J.P., Contreras-Reyes, E., Arriagada, C., 2018. Predicted path for hotspot tracks off South America since Paleocene times: tectonic implications of ridge-trench collision along the Andean margin. Gondwana Res. 64, 216–234.

Benioff, H., 1951. Global strain accumulation and release as revealed by great earthquakes. Geol. Soc. Am. Bull. 62 (4), 331–338. https://doi.org/10.1130/0016-7606(1951)62[331:GSAARA]2.0.CO;2.

Blot, C., 1981a. Deep root of andesitic volcanoes: new evidence of magma generation at depth in the Benioff zone. J. Volcanol. Geoth. Res. 10 (4), 339–364.

Blot, C., 1981b. Earthquakes at depth beneath volcanoes, forerunners of their activities. Application to White Island, New Zealand. J. Volcanol. Geoth. Res. 9 (4), 277–291.

Brantut, N., Stefanou, I., Sulem, J., 2017. Dehydration-induced instabilities at intermediate depths in subduction zones. J. Geophys. Res. Solid Earth 122 (8), 6087–6107.

Carbunar, O.F., Radulian, M., 2011. Geometrical constraints for the configuration of the Vrancea (Romania) intermediate-depth seismicity nest. J. Seismol. 15 (4), 579–598.

Carr, M.J., Stoiber, R.E., 1973. Intermediate depth earthquakes and volcanic eruptions in Central America, 1961–1972. Bull. Volcanol. 37 (3), 326–337.

Cesca, S., 2020. Seiscloud, a tool for density-based seismicity clustering and visualization. J. Seismol. 24 (3), 443–457.

Cesca, S., Heimann, S., Dahm, T., 2011. Rapid directivity detection by azimuthal amplitude spectra inversion. J. Seismol. 15, 147–164.

Cesca, S., Grigoli, F., Heimann, S., Dahm, T., Kriegerowski, M., Sobiesiak, M., Tassara, C., Olcay, M., 2016. The M w 8.1 2014 Iquique, Chile, seismic sequence: a tale of foreshocks and aftershocks. Geophys. J. Int. 204 (3), 1766–1780.

Comte, D., Pardo, M., 1991. Reappraisal of great historical earthquakes in the northern Chile and southern Peru seismic gaps. Nat. Hazards 4 (1), 23–44.

Contreras-Reyes, E., Osses, A., 2010. Lithospheric flexure modelling seaward of the Chile trench: implications for oceanic plate weakening in the Trench Outer Rise region. Geophys. J. Int. 182 (1), 97–112.

Contreras-Reyes, E., Díaz, D., Bello-González, J.P., Slezak, K., Potin, B., Comte, D., Maksymowicz, A., Ruiz, J.A., Oses, A., Ruiz, S., 2021. Subduction zone fluids and arc magmas conducted by lithospheric deformed regions beneath the central Andes. Sci. Rep. 11 (1), 1–12.

Dahm, T., Brandsdottir, B., 1997. Moment tensors of microearthquakes from the Eyjafjallajokull volcano in South Iceland. Geophys. J. Int. 130 (1), 183–192. https://doi.org/10.1111/j.1365–246X.1997.tb00997.x.

Delouis, B., Monfret, T., Dorbath, L., Pardo, M., Rivera, L., Comte, D., Haessler, H., Caminade, J.-P., Ponce, L., Kausel, E., Cisternas, A., 1997. The M w=8.0 Antofagasta (northern Chile) earthquake of 30 july 1995; A precursor to the end of the large 1877 gap. Bull. Seismol. Soc. Am. 87, 427–445.

Delouis, B., Pardo, M., Legrand, D., Monfret, T., 2009. The M w 7.7 Tocopilla earthquake of 14 November 2007 at the southern edge of the northern Chile seismic gap: rupture in the deep part of the coupled plate interface. Bull. Seismol. Soc. Am. 99 (1), 87–94.

Engdahl, E.R., 1977. Seismicity and plate subduction in the central Aleutians. Island Arcs. Deep Sea Trenches and Back-Arc Basins 1, 259–271.

Frohlich, C., 1989. The nature of deep-focus earthquakes. Annu. Rev. Earth Planet Sci. 17 (1), 227–254.

Frohlich, C., 2006. Deep Earthquakes.

Frohlich, C., Kadinsky-Cade, K., Davis, S.D., 1995. A reexamination of the Bucaramanga, Colombia, earthquake nest. Bull. Seismol. Soc. Am. 85 (6), 1622–1634.

Fukao, Y., 1972. Source process of a large deep-focus earthquake and its tectonic implications - the western Brazil earthquake of 1963. Phys. Earth Planet. In. 5, 61–76. https://doi.org/10.1016/0031-9201(72)90074-x.

Gao, Y., Tilmann, F., van Herwaarden, D.P., Thrastarson, S., Fichtner, A., Heit, B., Schurr, B.D., 2021a. Full waveform inversion beneath the central Andes: insight into the dehydration of the Nazca slab and delamination of the back-arc lithosphere. Earth and Space Science Open Archive ESSOAr.

Gao, Y., Yuan, X., Heit, B., Tilmann, F., van Herwaarden, D.P., Thrastarson, S., Schurr, B., 2021b. Impact of the Juan Fernandez ridge on the Pampean flat subduction inferred from full waveform inversion. Geophys. Res. Lett. 48 (21), e2021GL095509.

GFZ German Research Centre for Geosciences & Institut des Sciences de l'Univers-Centre National de la Recherche CNRS-INSU IPOC Seismic Network, 2006. Integrated Plate boundary observatory Chile—IPOC. Other/Seismic Network. https://doi.org/10.14470/PK615318.

Hacker, B.R., Peacock, S.M., Abers, G.A., Holloway, S.D., 2003. Subduction factory 2. Are intermediate-depth earthquakes in subducting slabs linked to metamorphic dehydration reactions? J. Geophys. Res. Solid Earth 108 (B1).

Hanks, T.C., Kanamori, H., 1979. A moment magnitude scale. J. Geophys. Res. Solid Earth 84 (B5), 2348–2350.

Hasegawa, A., Nakajima, J., 2017. Seismic imaging of slab metamorphism and genesis of intermediate-depth intraslab earthquakes. Prog. Earth Planet. Sci. 4 (1), 1–31.

Hayes, G.P., Herman, M.W., Barnhart, W.D., Furlong, K.P., Riquelme, S., Benz, H.M., Samsonov, S., 2014. Continuing megathrust earthquake potential in Chile after the 2014 Iquique earthquake. Nature 512 (7514), 295–298.

Hayes, G.P., Moore, G.L., Portner, D.E., Hearne, M., Flamme, H., Furtney, M., Smoczyk, G.M., 2018. Slab2, a comprehensive subduction zone geometry model. Science 362 (6410), 58–61.

Heimann, S., Isken, M., Kühn, D., Sudhaus, H., Steinberg, A., Vasyura-Bathke, H., Daout, S., Cesca, S., Dahm, T., 2018. Grond – a probabilistic earthquake source inversion framework. GFZ Data Services. https://doi.org/10.5880/GFZ.2.1.2018.003.

Heit, B., Bianchi, M., Yuan, X., Kay, S.M., Sandvol, E., Kumar, P., Kind, R., Alonso, R.N., Brown, L.D., Comte, D., 2014. Structure of the crust and the lithosphere beneath the southern Puna plateau from teleseismic receiver functions. Earth Planet Sci. Lett. 385, 1–11.

John, T., Medvedev, S., Rüpke, L.H., Andersen, T.B., Podladchikov, Y.Y., Austrheim, H., 2009. Generation of intermediate-depth earthquakes by self-localizing thermal runaway. Nat. Geosci. 2 (2), 137–140.

Jost, M.L., Hermann, R.B., 1989. A student's guide to and review of moment tensors. Seismol Res. Lett. 60, 37–57.

Jung, H., Green Ii, H.W., Dobrzhinetskaya, L.F., 2004. Intermediate-depth earthquake faulting by dehydration embrittlement with negative volume change. Nature 428 (6982), 545–549.

Kikuchi, M., Ishida, M., 1993. Source retrieval for deep local earthquakes with broadband records. Bull. Seismol. Soc. Am. 83, 1855–1870.

Kirby, S.H., Durham, W.B., Stern, L.A., 1991. Mantle phase changes and deep-earthquake faulting in subducting lithosphere. Science 252 (5003), 216–225.

Krüger, F., Hongn, F., 2016. Seismic neTwoRk/Array in norThwEstern Argentina. International Federation of Digital Seismograph Networks. https://doi.org/10.7914/SN/2S_2016.

Lemoine, A., Madariaga, R., Campos, J., 2002. Slab-pull and slab-push earthquakes in the Mexican, Chilean and Peruvian subduction zones. Phys. Earth Planet. In. 132 (1–3), 157–175.

Lister, G., Kennett, B., Richards, S., Forster, M., 2008. Boudinage of a stretching slablet implicated in earthquakes beneath the Hindu Kush. Nat. Geosci. 1 (3), 196–201.

López-Comino, J.A., Stich, D., Morales, J., Ferreira, A.M.G., 2016. Resolution of rupture directivity in weak events: 1-D versus 2-D source parameterizations for the 2011, Mw 4.6 and 5.2 Lorca earthquakes, Spain. J. Geophys. Res. Solid Earth 121, 6608–6626.

Maghsoudi, S., Hainzl, S., Cesca, S., Dahm, T., Kaiser, D., 2014. Identification and characterization of growing large-scale en-echelon fractures in a salt mine. Geophys. J. Int. 196 (2), 1092–1105. https://doi.org/10.1093/gji/ggt443.

Pavlis, G.L., Das, S., 2000. The Pamir-Hindu Kush seismic zone as a strain marker for flow in the upper mantle. Tectonics 19 (1), 103–115.

Pegler, G., Das, S., 1998. An enhanced image of the Pamir-Hindu Kush seismic zone from relocated earthquake hypocentres. Geophys. J. Int. 134 (2), 573–595.

Poli, P., Prieto, G., Rivera, E., Ruiz, S., 2016. Earthquakes initiation and thermal shear instability in the Hindu Kush intermediate depth nest. Geophys. Res. Lett. 43 (4), 1537–1542.

Prieto, G.A., Beroza, G.C., Barrett, S.A., López, G.A., Florez, M., 2012. Earthquake nests as natural laboratories for the study of intermediate-depth earthquake mechanics. Tectonophysics 570, 42–56.

Ruegg, J.C., Campos, J., Armijo, R., Barrientos, S., Briole, P., Thiele, R., Serrurier, L., 1996. The Mw= 8.1 Antofagasta (North Chile) earthquake of July 30, 1995: first results from teleseismic and geodetic data. Geophys. Res. Lett. 23 (9), 917–920.

Schneider, J.F., Pennington, W.D., Meyer, R.P., 1987. Microseismicity and focal mechanisms of the intermediate-depth Bucaramanga Nest, Colombia. J. Geophys. Res. Solid Earth 92 (B13), 13913–13926.

Schurr, B., Asch, G., Rietbrock, A., Trumbull, R., Haberland, C., 2003. Complex patterns of fluid and melt transport in the central Andean subduction zone revealed by attenuation tomography. Earth Planet Sci. Lett. 215 (1–2), 105–119.

Schurr, B., Asch, G., Rosenau, M., Wang, R., Oncken, O., Barrientos, S., Vilotte, J.P., 2012. The 2007 M7. 7 Tocopilla northern Chile earthquake sequence: implications for along-strike and downdip rupture segmentation and megathrust frictional behavior. J. Geophys. Res. Solid Earth 117 (B5).

Schurr, B., Asch, G., Hainzl, S., Bedford, J., Hoechner, A., Palo, M., Vilotte, J.P., 2014. Gradual unlocking of plate boundary controlled initiation of the 2014 Iquique earthquake. Nature 512 (7514), 299–302.

Sippl, C., Schurr, B., Asch, G., Kummerow, J., 2018. Seismicity structure of the northern Chile forearc from> 100,000 double-difference relocated hypocenters. J. Geophys. Res. Solid Earth 123 (5), 4063–4087.

Sippl, C., Schurr, B., Asch, G., Kummerow, J., 2018. Catalogue of Earthquake Hypocenters for Northern Chile Compiled from IPOC (plus auxiliary) seismic stations.

Tibi, R., Estabrook, C.H., Bock, G., 1999. The 1996 June 17 flores sea and 1994 March 9 Fiji-Tonga earthquakes: source processes and deep earthquake mechanisms. Geophys. J. Int. 138, 625–642. https://doi.org/10.1046/j.1365-246x.1999.00879.x.

Tryggvason, E., Lawson Jr., J.E., 1970. The intermediate earthquake source near Bucaramanga, Colombia. Bull. Seismol. Soc. Am. 60 (1), 269–276.

Utsu, T., Ogata, Y., 1995. The centenary of the Omori formula for a decay law of aftershock activity. J. Phys. Earth 43 (1), 1–33.

Vavryčuk, V., 2015. Moment tensor decompositions revisited. J. Seismol. 19 (1), 231–252.

Wagner, L.S., Okal, E.A., 2019. The Pucallpa nest and its constraints on the geometry of the Peruvian flat slab. Tectonophysics 762, 97–108.

Wells, D.L., Coppersmith, K.J., 1994. New empirical relationships among magnitude, rupture length, rupture width, rupture area, and surface displacement. Bull. Seismol. Soc. Am. 84 (4), 974–1002.

Yáñez, G.A., Ranero, C.R., von Huene, R., Díaz, J., 2001. Magnetic anomaly interpretation across the southern central Andes (32–34 S): the role of the Juan Fernández Ridge in the late Tertiary evolution of the margin. J. Geophys. Res. Solid Earth 106 (B4), 6325–6345.

Yuan, X., Sobolev, S.V., Kind, R., Oncken, O., Bock, G., Asch, G., Comte, D., 2000. Subduction and collision processes in the Central Andes constrained by converted seismic phases. Nature 408 (6815), 958–961.
Zarifi, Z., Havskov, J., 2003. Characteristics of dense nests of deep and intermediate-depth seismicity. Adv. Geophys. 46, 238–278.
Zarifi, Z., Havskov, J., Hanyga, A., 2007. An insight into the Bucaramanga nest. Tectonophysics 443 (1–2), 93–105. https://doi.org/10.1016/j.tecto.2007.06.004. ISSN 0040-1951.
Zeckra, M., Krüger, F., Aranda Viana, G., Criado Sutti, E., 2016. Seismic neTwoRk/Array in norThwEstern Argentina. International Federation of Digital Seismograph Networks. https://doi.org/10.7914/SN/2S_2016. Other/Seismic Network.

Data Availability Statement

GCMT (Lamont-Doherty Earth Observatory of Columbia University, USA), 2018. Ekström et al., 2012. https://www.globalcmt.org/. (Accessed December 2020).
GEOFON (Germany) event locations were obtained from the GEOFON program of the GFZ German Research Center for Geosciences using data from the GEVN partner networks, 2017. https://geofon.gfz-potsdam.de/eqinfo/list.php (last access. (Accessed December 2020).
Sippl et al., (2018) catalog, Sippl, C., Schurr, B., Asch, G., Kummerow, J., 2018. Seismicity structure of the northern Chile forearc from >100,000 double-difference relocated hypocenters. Journal of Geophysical Research: Solid Earth 123 (5), 4063–4087. https://doi.org/10.1002/2017jb015384.
CSN, 2018. Chile (last access: March 2020). http://www.sismologia.cl/.
GFZ & CNRS-INSU, 2006. IPOC Seismic Network. Integrated Plate boundary Observatory Chile – IPOC, 10.14470/ PK615318.
Martin, Zeckra, Frank, Krüger, Aranda Viana, Germán, , Emilio, Criado Sutti, J.M., 2016. Seismic neTwoRk/Array in norThwEstern arGentina. International Federation of Digital Seismograph Networks. https://doi.org/10.7914/SN/2S_2016. Other/Seismic Network.